

A Gaia DR 2 and VLT/FLAMES search for new satellites of the LMC[★]

T. K. Fritz^{1,2}, R. Carrera³, and G. Battaglia^{1,2}

¹ Instituto de Astrofísica de Canarias, calle Via Lactea s/n, E-38205 La Laguna, Tenerife, Spain
e-mail: tfritz@iac.es

² Universidad de La Laguna, Dpto. Astrofísica, E-38206 La Laguna, Tenerife, Spain

³ INAF - Osservatorio Astronomico di Padova, Padova, Italy

ABSTRACT

A wealth of tiny galactic systems populates the surroundings of the Milky Way. However, some of these objects might actually have their origin as former satellites of the Magellanic Clouds, in particular the LMC. An example of the importance of understanding how many systems are genuine satellites of the Milky Way or the LMC are the implications that the number and luminosity/mass function of satellites around hosts of different mass have for dark matter theories and treatment of baryonic physics in simulations of structure formation. Here we aim at deriving the bulk motions and estimates of the internal velocity dispersion and metallicity properties in four recently discovered southern dwarf galaxies, Columba I, Reticulum III, Phoenix II and Horologium II. We combine *Gaia* DR2 astrometric measurements and photometry to new FLAMES/GIRAFFE intermediate resolution spectroscopic data in the region of the nearIR Ca II triplet lines; such combination is essential for finding potential member stars in these low luminosity systems. We find very likely member stars in all four satellites and are able to determine (or place limits on) the systems bulk motions and average internal properties. The systems are found to be very metal-poor, in agreement with dwarf galaxies and dwarf galaxy candidates of similar luminosity. Among the four systems, the only one that we can place in the category of dwarf galaxies is Phoenix II given its resolved large velocity dispersion ($7.1^{+1.5}_{-1.1}$ km/s) and intrinsic metallicity spread (0.34 dex). The orbital pole of Phoenix II is well constrained and close to the orbital pole of the LMC, suggesting a prior association. The uncertainty on the orbital poles of the other systems are presently very large, and in the case of Horologium II dependent on the sample of members adopted, making an association not impossible.

Key words. Astrometry - Proper motions - Galaxies: dwarf - Galaxies: kinematics and dynamics - Local Group - Galaxies: evolution

1. Introduction

In the Λ Cold Dark Matter (Λ CDM) framework, also low mass halos are expected to host their own systems of satellite sub-halos, although how many of these will actually be luminous satellites depends on several factors, among which the mass of the host halo, the mass and build-up history of the sub-halos themselves and various environmental factors, including the strength of the UV-ionizing background (see e.g. the recent review by Bullock & Boylan-Kolchin 2017 and references therein).

Observationally, there have already been several detections of low-luminosity galaxies possibly physically associated to stellar systems of similar or lower stellar mass than the LMC (e.g. Antlia A and the recently discovered Antlia B around NGC 3109, (Sand et al. 2015), Scl-MM-Dw1 around NGC 253 (Sand et al. 2014)); in some cases, the "status" of satellite galaxy is guaranteed by the on-going tidal disruption of such systems (e.g. Rich et al. (2012), Amorisco et al. (2014), Annibali et al. (2016), Toloba et al. (2016)). This could in principle be interpreted as a qualitative confirmation of one of the predictions of the Λ CDM hierarchical formation framework.

Recently, about two dozens candidate low luminosity, dwarf galaxies were discovered often at projected locations in the sky close to the Magellanic Clouds (Drlica-Wagner et al. 2015a; Koposov et al. 2015a; Martin et al. 2015; Bechtol et al. 2015; Laevens et al. 2015; Drlica-Wagner et al. 2015b; Torrealba et al.

2018; Kim & Jerjen 2015; Kim et al. 2015; Koposov et al. 2018).

This has of course raised the question of whether some of these systems might be, or were before infall, part of a satellite system of the Clouds rather than the Milky Way (MW). Tackling how many, and which ones, of these dwarf galaxies might have been brought in by the Clouds would give insights into several aspects of galaxy formation in a cosmological context: besides improving the current observational information on the properties of satellite systems around galaxies of lower mass than the MW, it would allow to make further considerations into the efficiency of galaxy formation at the low-mass end (see e.g. Dooley et al. (2017)), and might imply a revision of our understanding of the properties of the MW satellite system itself, in terms of the number of its members, as well as its luminosity and circular velocity function. Identifying *which ones* of these dwarf galaxies in particular might be/have been associated to the Clouds gives also a direct avenue to start addressing the effects of group pre-processing onto the observed properties of dwarf galaxies from the detailed perspective of resolved stellar population studies.

There have been predictions on the number of satellites that could be associated to systems with stellar masses similar to the Magellanic Clouds, and in what stellar mass range they should be found (see. e.g. Dooley et al. (2017)). A conclusion from the aforementioned study is that there is a dearth of "massive" satellites around the LMC and SMC; this could imply a Magellanic-Clouds "missing satellite problem", although other solutions are possible, such as strong modifications to abundance-matching

[★] Based on ESO programs 096.B-0785(A) and 098.B-0419(A).

relations (which at the low mass end are indeed very uncertain, see e.g. Garrison-Kimmel et al. (2017), Revaz & Jablonka (2018) and references therein), strong tidal-stripping etc.

Several studies have instead focused on predicting which ones of the dwarf galaxies found in the surroundings of the Milky Way could have been brought in by the Magellanic system (Sales et al. 2011; Deason et al. 2015; Yozin & Bekki 2015; Jethwa et al. 2016; Sales et al. 2017).

Among these, Deason et al. (2015) used the ELVIS N-body simulations to identify LMC-mass sub-haloes of MW/M31-like systems (considering virial masses in the range broadly expected for the LMC, i.e. $1\text{--}3 \times 10^{11} M_{\odot}$) and showed that the system of satellites disperse rapidly in phase-space, unless the group has infallen recently. The sample of 25 LMC-analogs included three dynamical analogs (with similar radial and tangential velocity as observed for the LMC): the expectations in these cases are that the sub-haloes found at $z = 0$ within ~ 50 kpc, or with a 3D velocity differing less ~ 50 km/s, from the original host have more than 50% chance to have been part of a LMC-mass group. Nonetheless, for the whole sample considered together, systems within 50 kpc *and* 50 km/s of a LMC-mass dwarf at $z = 0$ would have $>90\%$ probability of having been former group members.

Sales et al. (2017) used the LMC-analog identified in Sales et al. (2011) in the Aquarius simulations, which has a pericenter and velocity in good agreement with the measurements, to test whether any of the 20 dwarfs known at the time in the vicinity of the LMC/SMC are/were associated to the Clouds. Among the systems that had no kinematic information, they found Hor II, Eri III, Ret III, Tuc IV, Tuc V and Phx II to have positions and distances consistent with a Magellanic origin, although they stressed kinematic information was needed to confirm the association. In this study, several objects (among which all the classical dSphs, apart the SMC) were excluded to have been brought in by the Clouds. However, the LMC-analog virial mass before infall ($M_{200} = 3.6 \times 10^{10} M_{\odot}$) is at the lower end of that expected from abundance matching relations or measurements of the LMC circular velocity (van der Marel & Kallivayalil 2014); the satellite system of a more massive LMC-analog would have probably have had an intrinsically larger velocity dispersion and more extended spatial distribution; this would likely result in a wider distribution in velocity and distance space at $z = 0$ for the debris of accreted material with respect to those analyzed in that study.

Jethwa et al. (2016) have built a dynamical model of the Magellanic system, which takes into account the dynamical influence of the SMC on the group satellites orbits, the dynamical friction exerted by the LMC onto the SMC, and by the MW on the Magellanic Clouds, and a non-static MW. The LMC masses explored encompass the range of those in Deason et al. (2015) and Sales et al. (2017). Assuming isotropy for the MW sub-halo system, they found that half of the 14 DES dwarfs they were considering had a probability >0.7 of having belonged to the LMC.

An important, general conclusion from the above works is that knowledge of the systemic radial velocities, combined to sky position and distance, can greatly aid in the identification of previous Magellanic Clouds satellites. In particular, the most compelling evidence for association is expected to be provided by the additional information afforded by knowledge of systemic proper motions; this is due to the fact that the accreted galaxies are expected to share a similar direction of the orbital angular momentum of the LMC.

With the second *Gaia* data release (Gaia Collaboration et al. 2018a), the situation has dramatically improved: not only have the accuracy of the systemic proper motions of the classical MW

dwarf spheroidal galaxies (dSphs)¹ been either significantly improved in several cases Gaia Collaboration et al. (2018b), but such determination has finally become possible for dozens of the ultra-faint dwarf galaxies (Fritz et al. 2018; Kallivayalil et al. 2018; Massari & Helmi 2018; Simon 2018), while before only Segue 1 had a systemic proper motion measurement (Fritz et al. 2017b). All of the above, being in a common, absolute reference system.

Kallivayalil et al. (2018) used the Sales et al. (2011, 2017) LMC-analog to test a possible association to the LMC for 32 UFD systems with $M_V \gtrsim -8$. For the systems for which 3D velocities could be obtained, given the additional availability of published spectroscopic data, they conclude that four of those (Hor I, Car II, Car III and Hyd I) were former satellites of the Clouds, while Hyd II and Dra II could be reconciled with a model allowing for a larger dispersion of the tidal debris properties in velocity and distance/sky location.

For the systems that were lacking either systemic proper motion and/or radial velocity measurements at the times of the studies, predictions are provided in several of the works cited above, under the assumption of a prior physical association to the Magellanic system. In particular, Jethwa et al. (2016) and Kallivayalil et al. (2018) provide such predictions in the observable space of proper motion and/or radial velocity measurements, which has the advantage of not carrying the error propagation in the conversion to Galactocentric velocities.

Here we present results from unpublished FLAMES/GIRAFFE intermediate resolution spectroscopic data available in the ESO archive for four faint satellites, found in the vicinity of the Clouds: Colomba I, Horologium II, Phoenix II and Reticulum III. These were discovered in DES data (Koposov et al. 2015a; Bechtol et al. 2015; Drlica-Wagner et al. 2015a; Kim & Jerjen 2015). Phx II was followed up with deeper Megacam imaging (Mutlu-Pakdil et al. 2018) and Col I with deeper Hyper Suprime-Cam imaging (Carlin et al. 2017). We use these in conjunction with *Gaia* DR2 astrometric information, to provide the first determination of the global properties (mean spectroscopic metallicity and line-of-sight velocity dispersion) and bulk motion of these systems, and make considerations on whether these four galaxies might have been former LMC satellites.

The paper is structured as follows: in Sect. 2 we describe the data-sets used for the analysis and detail the data-reduction procedure and determination of line-of-sight velocities and metallicities from the spectroscopic data; in Sect. 3 we describe the selection of stars members to the target systems and the determination of their global properties. In Sect. 4 we present the determination of space velocities and orbital properties of the objects in the sample, and give summary and conclusions in Sect. 5.

2. Data-sets

We analyse in this work four galaxies for which public FLAMES/GIRAFFE data exist in the ESO archive with no associated publication to this date: Columba I, Phoenix II, Horologium II and Reticulum III. We complement these with *Gaia* (Gaia Collaboration et al. 2016) data from the data release 2 (GDR2) (Gaia Collaboration et al. 2018a) and public DECam

¹ Even though they might simply be the same class of objects in most cases, we refer to the typically brighter, passively-evolving dwarf galaxies known prior to SDSS as "classical" dwarf spheroidal galaxies and to those discovered posterior to that as ultra-faint dwarfs (UFDs).

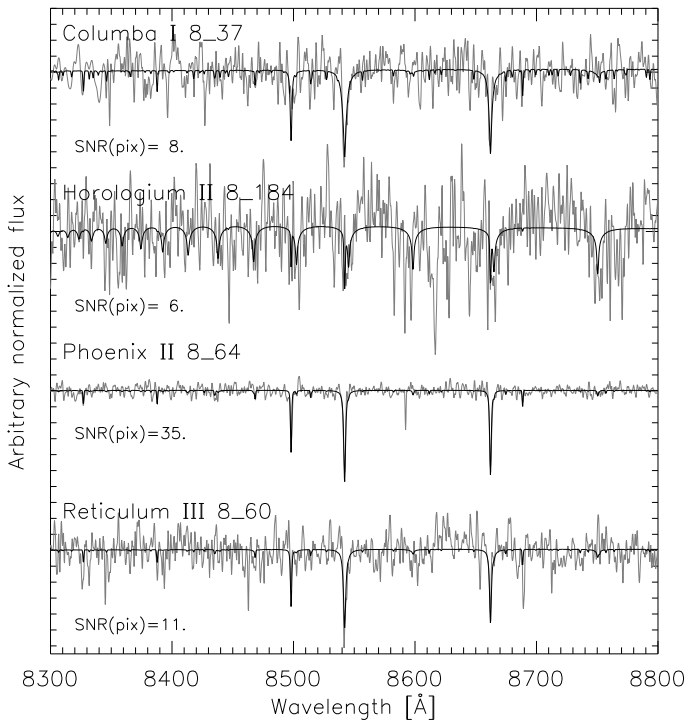


Fig. 1. Example of observed spectra (grey) with different SNR and the best synthetic models (black) found in the line-of-sight velocity determination analysis. Note that Horologium II 8_184 is a hot star, like a blue horizontal branch (BHB) star, and the continuum normalization is not optimized for these objects.

photometry of individual point-sources from the NOAO source catalog DR1 (Nidever et al. 2018).

2.1. Spectroscopic analysis

The spectroscopic observations were carried out with FLAMES mounted at Very Large Telescope (VLT) UT2 (Pasquini et al. 2002) using the grism LR8 that provides a resolution of ~ 6500 in the region of the near infrared Ca II triplet lines around 8500 Å. The observations consist of 3x3000s exposures for Phoenix II, 6x2775s for Columba I, 3x2775s for Horologium II and 3x2775s for Reticulum III.

These data have been processed through the GIRAFFE data-reduction pipeline (Melo et al. 2009). This pipeline performs the bias, flat field and scattered light corrections; finds, traces, and extracts the spectra; and obtains the wavelength calibration based on daytime calibration exposures. Our own software was used to subtract the sky emission following the procedure described in detail by Carrera et al. (2017). Briefly, a master sky is obtained by averaging all the spectra obtained from fibers located on sky positions. The resulting master sky spectrum and the spectra for each object are separated into two components: continuum and line. To obtain the continuum of both sky and object lines we used a nonlinear median filter with 3σ clipping. The line spectrum is obtained by subtracting the continuum. The sky- and object-line components are compared to search for the scale factor that minimizes the sky line residuals. In practice, this optimum scaling factor is the value that minimizes the sum of the absolute differences between the object-line and the sky-line multiplied by the scale factor, known as L1 norm. The object-continuum is added back to the sky subtracted object-line spec-

trum. Finally, the sky continuum is subtracted assuming that the scale factor is the same as for the sky-line component.

After applying the barycentric correction, individual spectra were averaged to obtain the combined spectrum for each star using the individual SNR as weight and an average sigma clipping rejection algorithm to remove deviant pixels. Those individual exposures with very low signal-to-noise ratio (SNR), i.e. $\text{SNR} < 3 \text{ pixel}^{-1}$, are rejected. This “combined” spectrum is then cross correlated with each individual exposure to remove small shifts between them. This procedure is repeated until convergence.

At this point, the “combined” spectrum is cross correlated with a grid of synthetic spectra. The details about the computation of this grid can be found at Allende Prieto et al. (2018). This grid has three dimensions: metallicity, $[\text{Fe}/\text{H}]$; effective temperature, T_{eff} ; and surface gravity, $\log g$. Metallicity ranges from -5.0 to +1.0 dex with a step of 0.5 dex. Temperature goes from 3500 to 6000 K with a step of 500 K. Finally, the gravity covers from $\log g = 0.0$ to 5.0 dex with a step of 1.0 dex. This implies that the grid contains 432 synthetic spectra. For the α -elements abundances the spectra were computed assuming $[\alpha/\text{Fe}] = 0.5$ dex for $[\text{Fe}/\text{H}] \leq -1.5$ dex, $[\alpha/\text{Fe}] = 0.0$ dex for $[\text{Fe}/\text{H}] \geq +0.0$ dex, and linear between them. The abundances of other elements were fixed to the Solar values and the microturbulence velocity was fixed to 1.5 km s^{-1} . Firstly, each spectrum is cross-correlated with a reference synthetic spectrum, which has the Arcturus parameters, to obtain an initial shift. After applying this initial shift, the observed spectrum is compared with the whole grid in order to identify the model parameters that best reproduces it through a χ^2 minimization using FERRE² (Allende Prieto et al. 2006). The best-fitting synthetic spectrum is cross-correlated again with the observed spectrum in order to refine the shift between both. Of course, Arcturus is not the ideal template for some of the target stars. However, after the first initial determination of the shift with Arcturus, our procedure converges by itself to appropriate templates for these objects. There are a few stars for which this procedure yields temperatures close to the edge of the synthetic spectra grid, 6000 K, suggesting that they may be hotter. For these particular cases, we repeated the procedure using another synthetic spectrum grid covering a temperature range between 5500 and 8500 K also with a step of 500 K. The other features of this grid are the same that the previous one except for the $\log g$, which starts at 1.0 dex. An example of the obtained fits is shown in Figure 1.

The shifts obtained for each individual exposure are applied to the “combined” line-of-sight velocity to obtain individual values for each exposure. The final heliocentric line-of-sight velocity is obtained as the average of these using the individual SNR as weight. The procedure followed allows also to determine the scatter between the multiple individual line-of-sight velocity determinations, V_{scatter} (see Fig. 2). This provides a better estimate of the internal precision than the typical uncertainty determined from the cross-correlation peak. However, we noticed that even at low SNR the procedure produces low V_{scatter} values. To better constrain the run of V_{scatter} as a function of SNR we therefore fit an exponential function to the individual values. According to this, the typical uncertainty at $\langle \text{SNR}_i \rangle \sim 10 \text{ pixel}^{-1}$ is $\sim 5 \text{ km s}^{-1}$.

The procedure followed to derive the line-of-sight velocities could potentially provide valuable information about the temperature, gravity, and metallicity of the observed stars. Unfortunately, the relatively small wavelength range covered, ~ 1000 Å between 8200 and 9200 Å, and the spectral resolution, ~ 6500 ,

² Available at <https://github.com/callendeprieto/ferre>

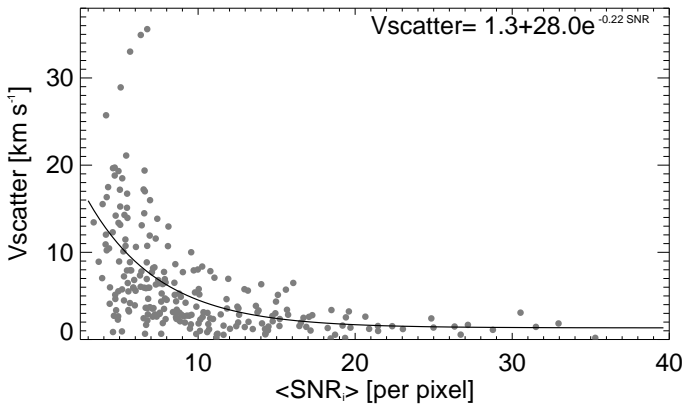


Fig. 2. Run of V_{scatter} as a function of median SNR of the individual exposures for all observed stars with at least 3 individual measurements. A exponential function, solid line, has been fitted to parameterize the distribution.

do not allow to properly constrain the temperature and gravity of the observed stars, which are however necessary for the determination of the stars's metallicity. Therefore, we use photometric information to constrain the stars's temperature and gravity. To that aim, we firstly transformed the Gaia magnitudes G , G_{BP} , and G_{RP} into V , I , J , H , and K_s using the relationships provided by Evans et al. (2018). The absolute magnitudes in these bandpasses have been obtained using the distances listed in Table 3. Temperatures have been derived using the relationships by Ramírez & Meléndez (2005) assuming and initial estimation of metallicity of $[\text{M}/\text{H}] = -2.0 \text{ dex}$. We derived temperatures for colors $V - I$, $V - J$, $V - H$, and $V - K_s$ independently. We have propagated the errors in all the procedure in other to constrain their uncertainties. The main sources of uncertainty are: the relationships to transform magnitudes from the Gaia photometric system and the uncertainty in the distance. All together, our temperatures have a typical uncertainty of 100 K. For the hottest stars the uncertainties are slightly higher. The values obtained from the different colors agree within the uncertainties. For this reason we obtained the final temperature by averaging the values derived for all colors for a given star.

Surface gravities have been determined using the Bayesian estimation algorithm³ presented by da Silva et al. (2006) with PARSEC evolutionary tracks (Bressan et al. 2012) and the temperatures obtained above. The average uncertainty in the $\log g$ determination is 0.15 dex. Finally, the metallicity has been determined by comparing the observed spectra with the same synthetic grid used in the line-of-sight velocity determination but fixing the temperatures and gravities to the photometric values. Our analysis confirms that one of the observed stars, horo2_8_184 is likely a blue horizontal branch star as expected from its position on the color-magnitude diagram (see Figures 4). The derived properties of potential member stars are shown in Table 1.

Owing to several of our observed stars having a low SNR, it is necessary to check the reliability of our results. To that aim, we selected synthetic models from the same grid as in the line-of-sight velocity determination, with metallicity $[\text{Fe}/\text{H}] = -2.0 \text{ dex}$ but with three different temperatures (4500, 5050, and 7500 K) and surface gravities (1.3, 2.0, and 3.5 dex), which covers the whole range of temperatures and gravities of the stars in our observed sample. Different levels of noise have been injected to each spectrum in order to obtain spectra of different SNRs. Fix-

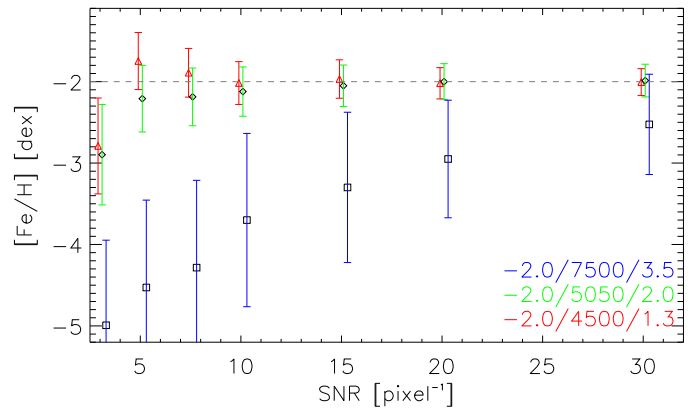


Fig. 3. Recovered metallicities as a function of SNR for three different synthetic spectra with the input stellar parameters listed on bottom-right corner ([Fe/H]/effective temperature/logg). Note that the SNR for each model has been slightly shifted to avoid superposition of the symbols.

ing the temperature and gravity to their input values, the spectra have been analyzed as the observed stars in order to determine the metallicity. Figure 3 shows the recovered metallicities as a function of the SNR. For $\text{SNR} = 3 \text{ pixel}^{-1}$, the recovered metallicity are underestimated with respect to the input one for the three models. From $\text{SNR} = 5 \text{ pixel}^{-1}$ the input metallicity is recovered within the uncertainties for the two coldest models. In fact, for the coldest model the method works slightly better than for the other one at a given SNR. For the hottest model, which represents the blue horizontal branch star in Horologium II (see Sect. 3), the recovered metallicities are always underestimated, although the difference with the input metallicity decreases as SNR increases.

3. Derivation of satellite properties

First, we concentrate on stars that have kinematic information from both GDR2 data and FLAMES observations because they greatly help each other to identify signals in the low number regime. We use similar criteria as in Fritz et al. (2018) to define a sample of halo stars. Since the stars at the distances of our targets are expected to have parallaxes consistent with zero, we require that the parallax has less than 2σ significance; this also removes stars with artificially very negative parallax (Lindegren et al. 2018). We further select stars by requiring them to be bound to the Milky Way given their proper motion at the distance of the galaxy. We use the same generous 2σ criterion as in Fritz et al. (2018). This selection based on kinematics greatly cleans the sample (for example for Phoenix II from 70 to 7 stars): as it can be appreciated in Figures 4-7, the disc component is essentially weeded out.

We then perform a broad selection on the colour-magnitude diagram (CMD) around the locus expected for red giant branch (RGB) and horizontal branch (HB) stars by using the Gaia G magnitudes and BP-RP colours. This retains nearly all FLAMES targets for Col I and Ret III, because they were originally targeted with a similar selection. In the case of Horo II and Phoenix II, the original selection did not appear to include a colour cut, therefore the number of stars is clearly reduced. In addition we use DECam colors qualitatively to be more certain about the position of faint stars on the CMD.

For the stars passing the above selection criteria, we inspect their location on the heliocentric line-of-sight velocity versus projected elliptical radius/half-light radius (r_{half}) plane: in all

³ Available at http://stev.oapd.inaf.it/cgi-bin/param_1.3

Table 1. Observed properties for potential member stars. Column 1 lists the star name, col. 2 and 3 its position on the sky, col.4 the distance from the galaxy center in units of projected half light radii, col. 5 and 6 give NSC DR1 DECam magnitudes in g- and i-bands, col. 7 the SNR of the spectrum in the combined spectrum, col. 8 and 9 the heliocentric velocity and metallicity derived from the FLAMES spectra, col. 10 and 11 the measured proper motions from Gaia DR2 data, col. 12 whether the star is considered as very likely (1) or possible member (0.5). The non members are only shown in the electronic table.

name	R.A.	Dec.	R/R_{half}	m_g	m_i	SNR	v_{helio}	[Fe/H]	$\mu_{\alpha^*} [\text{mas/yr}]$	$\mu_{\delta} [\text{mas/yr}]$	mem
coll_8_16	82.8243	-28.0539	1.25	21.39	20.24	6.1	149 ± 11.5	-1.9 ± 0.21			0.5
coll_8_29	82.8442	-28.0301	0.44	21.79	20.87	4.2	160.7 ± 13.2	-2.06 ± 0.3			1
coll_8_32	82.853	-28.0272	0.21	21.63	20.69	5	161.6 ± 12.6	-2.31 ± 0.23			1
coll_8_34	82.874	-28.0301	0.39	20.95	19.85	9.4	153.5 ± 9.4	-2.11 ± 0.15	-0.32 ± 0.87	0.23 ± 0.99	1
coll_8_37	82.8217	-27.9958	1.52	21.22	20.21	7.8	135.1 ± 10.5	-1.67 ± 0.15	-0.23 ± 1.1	0.8 ± 1.34	0.5
coll_8_61	82.9811	-28.0837	3.78	21.23	20.48	5.5	132.5 ± 12.2	-2.17 ± 0.24	0.59 ± 1.35	0.02 ± 1.91	0.5
coll_8_66	82.88	-28.039	0.62	19.85	18.61	18.5	154.9 ± 5.2	-2.36 ± 0.16	0.41 ± 0.3	-0.49 ± 0.42	1
coll_8_75	82.9846	-27.9753	3.88	21.04	20.01	7.9	137.8 ± 10.6	-1.64 ± 0.15	0.85 ± 0.92	-1.62 ± 0.94	0.5
horo2_2_48	49.3378	-50.0613	4.36	19.21	18.51	16.5	163.4 ± 6.3	-1.79 ± 0.16	1.7 ± 0.27	-0.47 ± 0.42	0.5
horo2_8_156	49.1365	-50.0215	0.13	21.4	20.7	5.7	189.5 ± 11.3	-2 ± 0.26	4.65 ± 2.94	1.48 ± 4.07	1
horo2_8_184	49.064	-50.0318	2.07	19.95	20.18	5.9	158.3 ± 10.8	-3.79 ± 2.45	0.12 ± 0.7	-0.65 ± 1.12	1
phx2_5_46	354.977	-54.4052	0.57	19.5	18.47	19.8	39 ± 4.3	-2.91 ± 0.16	0.54 ± 0.28	-1.69 ± 0.33	1
phx2_8_127	355.033	-54.3918	1.78	19.47	18.67	19.8	43.7 ± 4.2	-3.29 ± 0.18	0.59 ± 0.29	-1.03 ± 0.36	1
phx2_8_141	355.009	-54.374	1.71	21.24	20.51	6.7	17.3 ± 9.1	-2.48 ± 0.24	-1.99 ± 1.43	0.26 ± 2.19	1
phx2_8_24	354.93	-54.4229	2.72	20.21	19.97	7.5	26 ± 9.7	-1.01 ± 0.17	-0.24 ± 0.86	-1.9 ± 0.9	0.5
phx2_8_27	354.947	-54.4128	1.82	21.44	20.64	5.4	25.2 ± 11.2	-2.26 ± 0.24	0.63 ± 2.26	-1.96 ± 2.66	1
phx2_8_64	354.982	-54.369	1.54	18.63	17.51	34.6	28.9 ± 2.2	-2.7 ± 0.13	0.49 ± 0.15	-1.06 ± 0.17	1
ret3_2_70	56.2472	-60.4242	1.53	20.76	20.26	7.2	274.3 ± 10.3	-2.96 ± 0.48	3.34 ± 1.72	-1.51 ± 1.95	1
ret3_8_60	56.3902	-60.4491	0.37	20.63	19.75	11.3	273.3 ± 8.1	-2.61 ± 0.11	-0.78 ± 0.89	-1.05 ± 1.12	1
ret3_8_61	56.3604	-60.4523	0.06	20.24	19.3	14.8	275 ± 6.4	-3.18 ± 0.13	-0.78 ± 0.72	0.3 ± 0.83	1

cases some small group of stars clump at fairly similar velocity. This will be considered as our preliminary heliocentric line-of-sight systemic velocity for the galaxies, $v_{\text{helio,gal}}$. The velocity spike consists of 3 stars for Columba I, 3 (2) for Horologium II, 6 for Phoenix II and 3 for Reticulum III.

The first step is to determine whether the overall detection of an v_{helio} spike for a galaxy is robust. To that aim we determine the density of contaminant objects that will pass the above parallax, proper motion and CMD-based selection criteria (ρ_{back}) by applying the same cuts to GDR2 sources outside of 5 half light radii and inside of 10 half light radii. When determining the amount of expected contaminants, we also need to take into account that it is possible that not all potential targets had FLAMES/GIRAFFE fibers allocated on them. For that we select from the NSC DR1 catalog stars with magnitudes and colours consistent with being on the RGB or HB of the target galaxy. The faint limit is set by the faintest stars with Gaia kinematics, while the bright limit by the brightest star targeted by FLAMES. We also select stars in the same way from the FLAMES catalog. We then count in both catalogs how many stars are within 3 r_{half} and obtain a rough number for the completeness: $c = N_{\text{FLAMES}}/N_{\text{DECam}}$. c is between 67% and 85%.

Finally, we translate the radius into the corresponding area on the sky and multiply with ρ_{back} and c to obtain the number of expected background stars for each galaxy, N_{back} . We obtain 2.1 for Columba I, 5.4 for Horologium II, 1.4 for Phoenix II and 2.1 for Reticulum III. The larger number for Horologium II is caused by a star at 4.4 half light radii, when this rather bright star is omitted 1.2 stars are expected. Thus, in most cases the observed number of stars in the velocity spike is already somewhat larger than the expected number of contaminant stars at all velocities, indicating a detection.

Clearly, the number of expected contaminants will be much smaller when considering the velocity range occupied by the velocity "spike". Since no *Gaia* DR2 information on line-of-sight

velocity is available for sources as faint as those here studied, we aid our analysis with the *Gaia* mock catalog of Rybizki et al. (2018): we select objects within a 1° radius around the galaxies, produce new estimates of their parallax, proper motion and photometric properties by factoring in the measurement errors, and finally apply the selection criteria as on the data to these mock stars. The line-of-sight velocity distribution so obtained is broad and shows no sign of a disk population. Finally, we select mock stars within ± 50 km/s from the preliminary heliocentric velocity of each galaxy and fit this histogram with a quadratic function to obtain which fraction of stars has a velocity within ± 5 km/s of the velocity of the galaxy (f_{hel})

We then calculate by using Poisson statistics how often we should observe at least N_{back} in a given velocity range. To consider that we could have observed the "spike" at any velocity, we make the assumption that f_{hel} is constant as a function of heliocentric velocity for halo stars, and multiply N_{back} by the approximate velocity range covered by the spectroscopically observed stars (300km/s) and divide by the velocity range covered by stars in the "spikes". For all satellites, the likelihood to observe a spike of those numbers by chance is less than 0.1%, apart from Horo II, for which it is anyway small (2.4%).

The realness of the spike of Horo II could be doubted because the two potential member stars are separated by 31.2 km/s or 2 σ . However, one of the two stars has the color and magnitude of an BHB star exactly at the distance of the galaxy (80 kpc). At that distance, the density of stars with BHB-like colors (which could also be blue straggler stars) is very low, about 0.05 stars per square degree at 0.2 mag bin, when QSOs and White dwarfs are excluded (Deason et al. 2014). The BHB candidate is found in the inner 0.017 square degree around the galaxy position, thus there is less than 0.1% probability that the star is not associated to Horo II. Secondly, there is another brighter star within 5 km/s of the velocity of the BHB star at 4.4 half light radii. Due to its brightness there are only 0.5 stars expected even

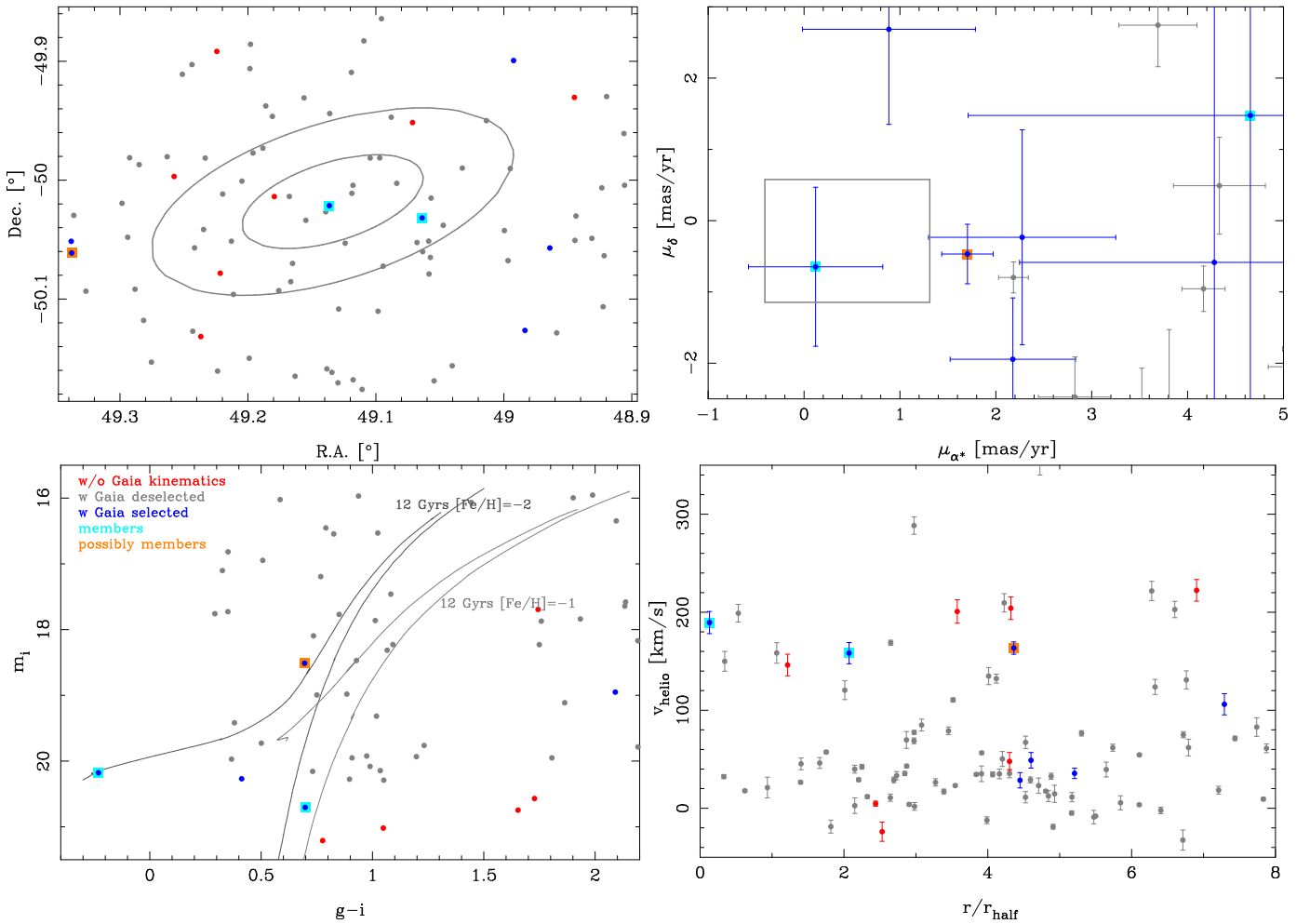


Fig. 4. Plots for the identification of the Horologium II members for targets with FLAMES spectroscopic observations. Stars consistent with a distant halo origin in Gaia parallax and proper motions are plotted in blue, the others in grey. Stars without Gaia proper motion information are plotted in red. The very likely members of the galaxy are enclosed within a cyan square, while the additional potential members within an orange square. Top left: spatial distribution of the targets. The ellipses have semi-major axis equal to 1.5 and 3 projected (elliptical) half light radii and use ellipticity and P.A. from Kim et al. (2015). Top right: location in the proper motion plane; the proper motion selection box given by the escape speed criterion is shown in gray; members are required to be consistent with it at least at the 2σ level. Bottom left: colour-magnitude diagram, with overlaid Parsec isochrones with $[Fe/H] = -2.0$ and -1.0 and age = 12 Gyr. The isochrones have solar-scaled $[\alpha/Fe]$; this might be a potential source for the discrepancy in the location of stars of a given spectroscopically determined metallicity with the isochrones of similar $[Fe/H]$, since stars in such ancient systems are typically α -enhanced (e.g. Mashonkina et al. 2017, and references therein). Bottom right: distribution on the line-of-sight v_{helio} versus distance from the galaxy center in units of projected elliptical half-light radius.

in this correspondingly larger area. Since now the velocity of system is already known even for a single star the probability for a chance association is slightly less than 1%. Therefore we use this star for our estimates of the mean properties of Horo II, although we also provide values when excluding this object. The star also strengthens the detection of the systemic velocity of Horo II.

Now we concentrate on the different question of whether a certain star is a polluter versus a member of the galaxy. We again use the Gaia data at larger distances (split into different magnitude bins, to account for different numbers of contaminants as a function of magnitude, i.e. brighter than $m_G = 19$, $19 < m_G < 20$ and $m_G > 20$) and the model for the heliocentric line-of-sight velocity distribution. We calculate the expected background level for each candidate star with the following formula:

$$n_{\text{back}} = f_{\text{hel}} \rho_{\text{back}} \pi r_{\text{star}}^2 \sqrt{[(v_{\text{hel,star}} - v_{\text{hel,gal}})^2 + 3^2] / 10}.$$

The 3 (km/s) accounts for some dispersion caused variation around the observed heliocentric velocity of the star, while the 10

removes the 10 km/s range previously used to determine f_{hel} . We use n_{back} to classify stars: in the following, stars with $n_{\text{back}} < 0.1$ are treated as very likely members, while sources with n_{back} between 0.1 and 1 are added as potential members in our secondary estimates of the properties of the systems.

The mentioned star at $4.4 r_{\text{half}}$ in Horo II is still classified only as candidate member. A star in Phoenix II at $2.8 r_{\text{half}}$ is formally a member with $n_{\text{back}} = 0.085$ but has a unusual high metallicity (see Tab. 1), therefore we consider it as candidate member, rather than a very likely member. In total we get 12 very likely members (2 in Col I, 2 in Horo II, 5 in Phx II, 3 in Ret III) at most within $2.1 r_{\text{half}}$ (without the aforementioned BHB star, the largest distance would be at $1.8 r_{\text{half}}$). In addition we have 5 candidates, 3 for Col I, 1 for Horo II and 1 for Phx II, usually at larger distances.

As a further step, we also consider the stars with FLAMES spectroscopic measurements but without *Gaia* kinematic information (see red symbols in Figs. 3-6). Only Col I has clearly promising candidates, therefore we ignore the other satellites.

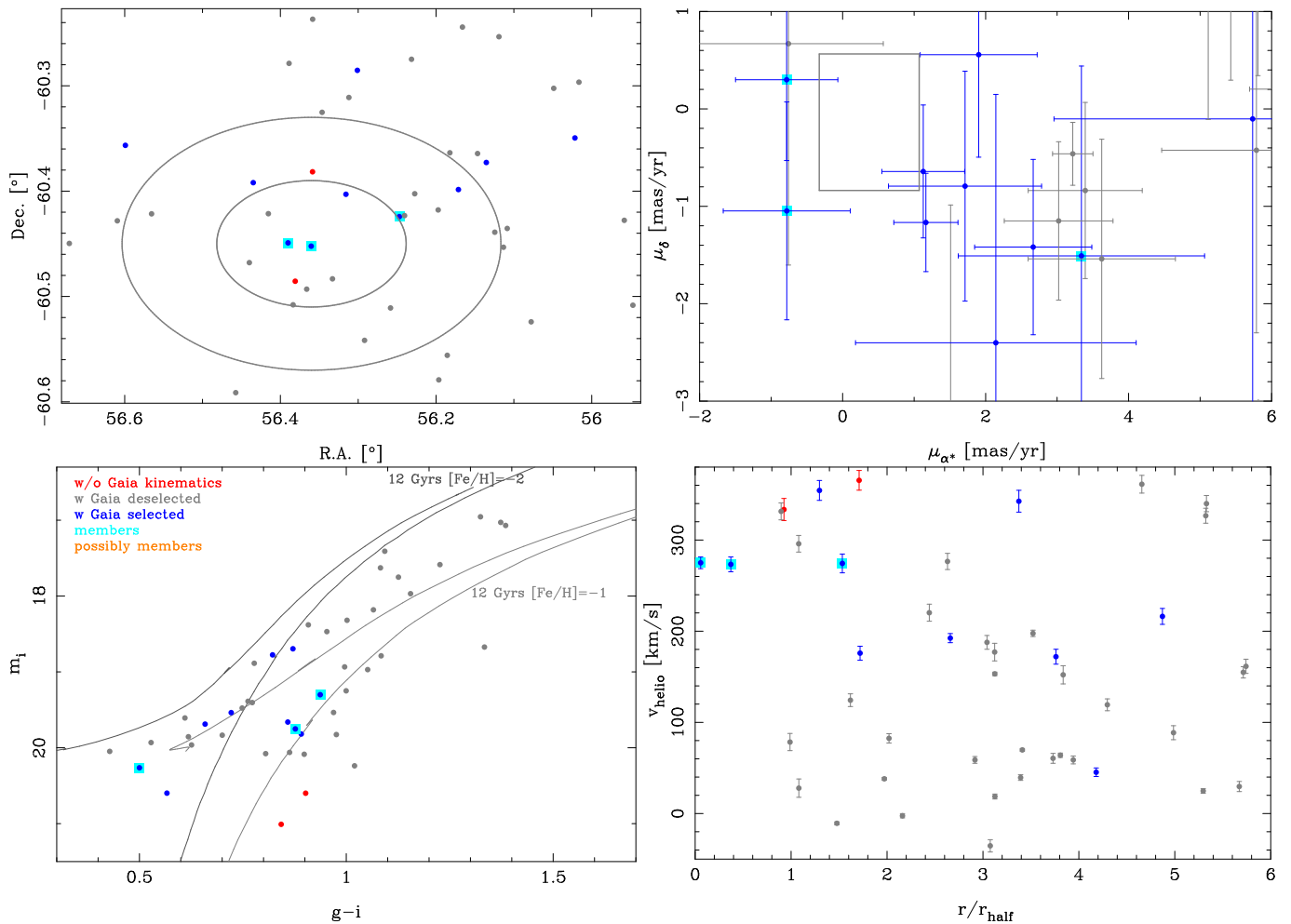


Fig. 5. As Figure 4, but for Reticulum III. The structural parameters are from Drlica-Wagner et al. (2015a).

We use the NSC catalog to determine the background density between $5 r_{\text{half}}$ and 0.5° using the color box of Col I for m_i between 20.4 and 21.5 and then use the line-of-sight velocity information as before: the three innermost stars have less than 3% probability to be contaminants and thus we add them to our sample of likely members. The outer most star has a $\sim 3\%$ probability of being a contaminant but it is also significantly redder than the other stars in the CMD; we therefore reclassify it as a candidate. We should note that the inclusion or exclusion of these new members to the sample does not significantly influence the overall properties of the system (determined taking into account error-bars) given the low SNR and large measurement errors of these faint stars. In total we have 4 very likely and three possible members for Columba I.

Table 1 lists the classification of a given star as a very likely member or candidate, together to its line-of-sight heliocentric velocity, $[\text{Fe}/\text{H}]$ and, when available, proper motion information.

3.1. Average properties of the satellites

After having selected which stars are members, we calculate the average properties of the object, namely the systemic proper motions in right ascension (μ_{α^*}) and declination (μ_δ), as well as the average correlation coefficient between μ_{α^*} and μ_δ by taking an error weighted average of all the member stars. We also calculate the average V_{helio} and $[\text{Fe}/\text{H}]$.

While the proper motions of the different stars agree given the large errors, this is not necessarily the case for V_{helio} and $[\text{Fe}/\text{H}]$; however, this is not surprising since galaxies are known (or defined, see Willman & Strader (2012)) to have a dispersion in these properties. Therefore, we fit also for the dispersions which we add in quadrature to the measurement errors; the error in the average properties quoted in the tables takes the dispersion into account. The global properties are derived both for the sample of very likely members only, and for the sample that includes also potential members (see Tab. 2, in which we also highlight our preferred cases, as in the explanations below).

Our independent measurement of the proper motion for Phoenix II is in excellent agreement with the measurement by Kallivayalil et al. (2018), which was guided by the predictions from the model postulating an association to the LMC. In case of Phoenix II, the star with uncertain membership has a metallicity ($[\text{Fe}/\text{H}] = -1.0 \pm 0.2$) significantly larger than the rest (see Fig. 8), thus we exclude it from the preferred values.

Also in the case of Col I the three less likely member have a somewhat larger metallicity, but of 0.3 to 0.6 dex higher than the rest, which could still be compatible with the intrinsic metallicity spread expected in these tiny galaxies (see e.g. Kirby et al. 2013; Frebel et al. 2014). The dispersion in line-of-sight velocity and metallicity determined from this sample of likely+candidate members can be seen as an upper limit in the dispersion of both quantities; we also note that without these three stars both dispersions would be consistent with zero).

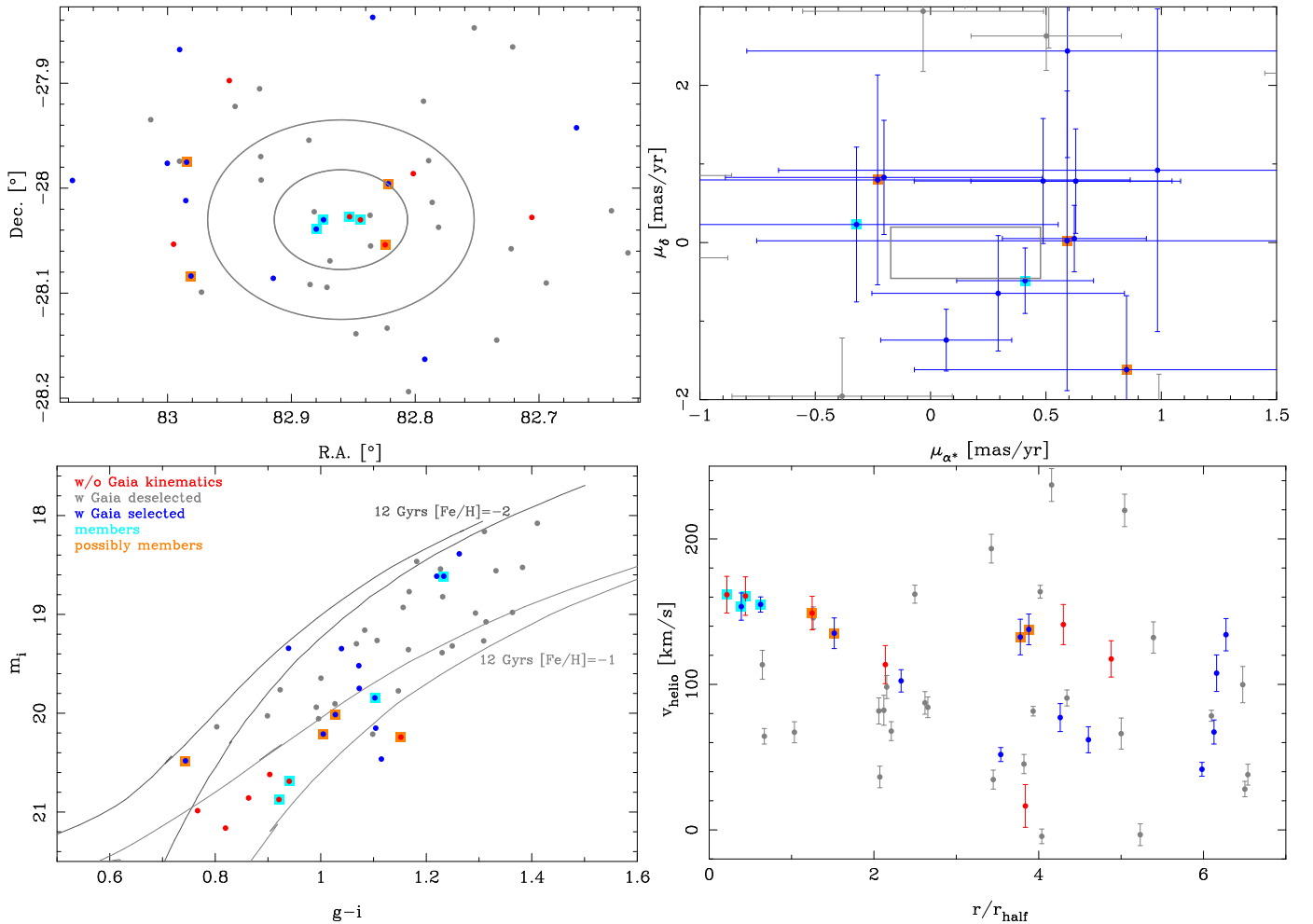


Fig. 6. As Figure 4, but for Columba I. The structural parameters are from Drlica-Wagner et al. (2015a).

For both Col I and Phoenix II, the difference in the proper motion value does not depend much on the sample used because the uncertain members have larger measurement errors and have therefore much less weight in the (weighted) average value. On the other hand, when including the uncertain member of Horo II, the dispersion in V_{helio} becomes smaller; since it is rather unlikely to have such a bright star by chance close to Horo II, this could be a hint that this star is a genuine member and we thus prefer values obtained with it.

Formally, we resolve the line-of-sight velocity dispersions in Horo II and Phx II. In case of Horo II it is only due to one outlier with a rather large velocity error, thus the determination does not appear robust to errors (and of course, also not to the presence of a possible binary star). In contrast, the value for Phx II (8 km/s) is more robust, because it is based on at least five stars which are partly so bright that a chance association is very unlikely. Binaries could still inflate the value, but it was shown that they usually do not cause such a large signal (McConnachie & Côté 2010). Nonetheless, it is clear that a robust determination of the intrinsic velocity dispersion would benefit from larger sample sizes and multiple observations with different time samplings.

For the full sample of very likely and candidate members in Col I we measure formally a metallicity dispersion of 0.21 dex but that is likely an upper limit given the possible presence of contaminants. For Ret III we measure a formally robust dispersion of 0.26 dex, but since the stars are rather faint, it is too

weak for a solid detection. Again the measurement for Phx II is the most robust one since the dispersion is 0.34dex, even in the case of only very likely members, and because it contains the brightest (highest SNR) stars. We note that phoenix2_8_127 ($m_G = 18.9$) has with $[\text{Fe}/\text{H}] = -3.28$ a remarkable low metallicity.

Overall, the values of the line-of-sight velocity and metallicity dispersions for Phx II are rather clear evidence that this is a galaxy. For the other three objects, some show signs of being galaxies, and none has upper limits which exclude a nature as galaxies, but their samples have small number statistics and properties that prevent a definite conclusion. We note however that, even if they are globular clusters, it is likely that they originated within a dwarf galaxy, since halo globulars were very likely accreted (Zinn 1993; Muratov & Gnedin 2010). Thus, even in this case we might still learn about the orbital properties of their former hosts. We note that all our targets have smaller metallicities than most halo globulars, which is unlike Laevens 1 (Weisz et al. 2016; Kirby et al. 2015) and Pyxis (Fritz et al. 2017a). This could very tentatively suggest an origin in a smaller system, although it is known that globular clusters can be much more metal-poor than the field stars of their host (as in the case of the Fornax dSph).

Finally, we note that the location of the member stars on the CMD appears to be too red with respect to the location expected from Padua isocrones of the same metallicity. We have checked that the same effect is visible in NSC DR1 photometry of the

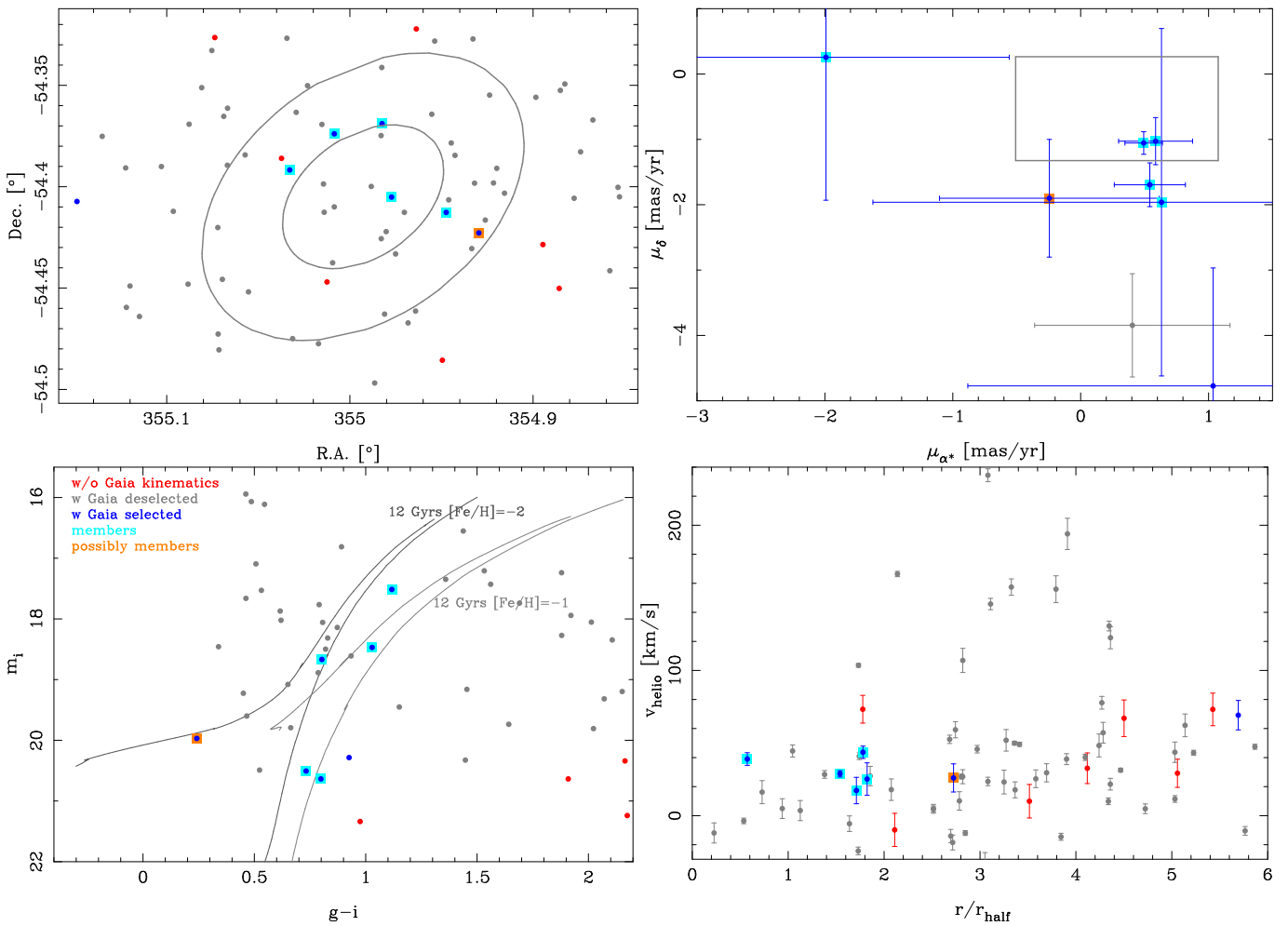


Fig. 7. As Figure 4, but for Phoenix II. The structural parameters are from Mutlu-Pakdil et al. (2018).

globular cluster NGC1904, and therefore it is not intrinsic to our analysis; also we note that Dartmouth isocrones of the same metallicity and age would lead to slightly redder colours than the Padua ones.

4. Velocities and orbital parameters

We now use the systemic proper motions and line-of-sight velocities derived in the previous section to determine the Galactocentric velocities and orbital parameters of the galaxies in the sample.

For the conversion into velocities, and for the following analysis, we also add to the proper motions errors in both dimensions a systematic error of 0.035 mas/yr (see Gaia Collaboration et al. (2018b)), which we assume to be uncorrelated between α and δ . Given the large random errors for our stars, the systematics are not important.

We followed the same procedure as Fritz et al. (2018) to convert the observed heliocentric velocities and proper motions into Galactocentric properties. This also accounts for uncertainties into the solar motion and distance of the galaxy, but in our cases the total uncertainties are dominated by the proper motion uncertainties. To estimate the uncertainties we run 20000 Monte Carlo simulations per satellite, considering also the correlation between the two proper motion dimensions; we repeat the exercise for the two sample of members (likely and likely+candidates), and provide both estimates in Tab. 3.

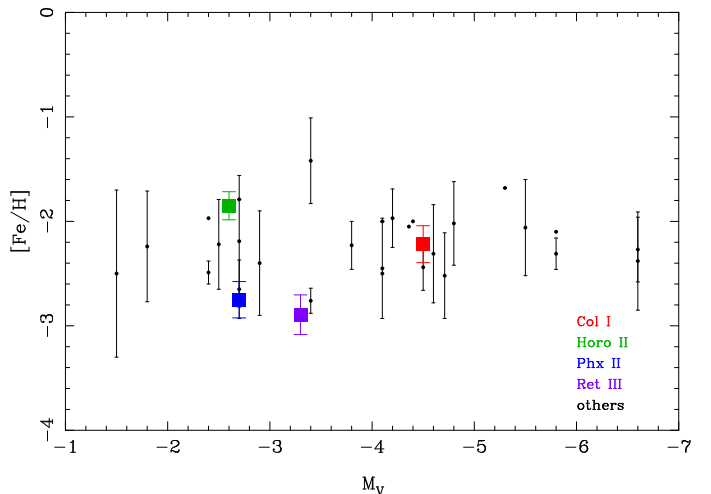


Fig. 8. Average metallicity and dispersion as a function of absolute magnitude for the four target satellites. For Col I and Horo II the dispersion is probably an upper limit. The metallicities for the "other objects" are from Torrealba et al. (2016); Martin et al. (2007); Simon & Geha (2007); Koch et al. (2009); Carlin et al. (2009); Li et al. (2018b); Kirby et al. (2015); Martin et al. (2016); Li et al. (2017); Walker et al. (2016); Koposov et al. (2015b); Walker et al. (2009); Kim et al. (2016); Simon et al. (2015, 2011); Kirby et al. (2013, 2017); Simon et al. (2017); Li et al. (2018a); Koposov et al. (2018); Willman et al. (2011). The point at $M_V = -5.3$, $[Fe/H] = -1.68$ is Laevens 1/Crater I which is probably a globular cluster.

Table 2. Average and global properties of the objects in our sample. Column 1 lists the object name, col. 2 and 3 the average heliocentric velocity and its dispersion, col.4 and 5 give the measured proper motion, col. 6 the average correlation coefficient between them, col. 7 and 8 the average metallicity and its dispersion. Above the line we show the values calculated from all possible members, below only from the certain members. We indicate in bold which determination we prefer (see main text for details).

satellite	$\langle V_{\text{helio}} \rangle [\text{km/s}]$	$\sigma V_{\text{helio}} [\text{km/s}]$	$\mu_\alpha^* [\text{mas/yr}]$	$\mu_\delta [\text{mas/yr}]$	$C_{\mu_\alpha^*, \mu_\delta}$	$\langle [Fe/H] \rangle$	$\sigma [Fe/H]$
Columba I	149.4 ± 3.6	< 5.6	0.35 ± 0.26	-0.45 ± 0.34	-0.13	-2.01 ± 0.1	$0.21^{+0.03}_{-0.02}$
Horologium II	169.4 ± 9.2	$12.9^{+8.5}_{-4.4}$	1.52 ± 0.25	-0.47 ± 0.39	0.07	-1.85 ± 0.13	< 0.12
Phoenix II	32.4 ± 3.9	$7.1^{+1.5}_{-1.1}$	0.49 ± 0.12	-1.18 ± 0.14	-0.47	-2.44 ± 0.32	$0.77^{+0.09}_{-0.07}$
Reticulum III	274.3 ± 4.5	< 3	-0.39 ± 0.53	-0.32 ± 0.63	0.45	-2.89 ± 0.19	$0.26^{+0.13}_{-0.06}$
Columba I	155.9 ± 4.1	< 5	0.33 ± 0.28	-0.38 ± 0.38	-0.14	-2.22 ± 0.18	< 0.20
Horologium II	173.7 ± 15.8	< 30	0.36 ± 0.68	-0.5 ± 1.08	-0.17	-1.85 ± 0.13	< 2
Phoenix II	32.9 ± 4.5	$8.2^{+1.9}_{-1.5}$	0.5 ± 0.12	-1.16 ± 0.14	-0.47	-2.75 ± 0.17	$0.34^{+0.07}_{-0.05}$

Table 3. Distances and velocities of satellites in our sample. Col 1 shows the name, col.2 the object Galactocentric distance, col.3, 4 and 5 give the Galactocentric radial, tangential and 3D velocity, respectively. In the top part we provide the determination from the full sample of members, while in the bottom part using the very likely members. We indicate in boldface our preferred value. Since both V_{tang} and V_{3D} are defined positive, the values we provide are deconvolved from the errors (the error-bars come from 16th and 84th percentiles of the distribution from the Monte Carlo simulations); this is a simplified way to take into account the fact that these quantities suffer to a larger extent of being inflated by the large measurement errors on the proper motions.

satellite	$d_{\text{GC}} [\text{kpc}]$	$V_{\text{rad}} [\text{km/s}]$	$V_{\text{tan}} [\text{km/s}]$	$V_{3D} [\text{km/s}]$
Col I	187	-40 ± 12	228^{+233}_{-228}	231^{+233}_{-203}
Horo II	79	34 ± 17	389 ± 98	390 ± 99
Phx II	80	-43 ± 6	261 ± 65	265 ± 65
Ret III	92	77 ± 28	270 ± 220	281 ± 222
Col I	187	-31 ± 13	126^{+233}_{-126}	130^{+233}_{-112}
Horo II	79	14 ± 39	0^{+228}_{-228}	14^{+231}_{-14}
Phx II	80	-42 ± 6	255 ± 67	258 ± 67

Due to the large errors in the proper motions, inferring the true values of the Galactocentric velocities is not trivial since the measurement errors are of similar size as the expected measurement. In the easier case of not positive definite values, we use the most likely value of the measurement to which we add the differences between the median and the 1σ quantiles in the MC simulations. For positive definite values like V_{3D} and the tangential velocity V_{tang} , we "deconvolve" the values obtained from the observed mean bulk motion of the system removing in quadrature (from V_{tang}^2) the mean of the error from the 16th and 84th percentiles of the Monte Carlo simulations, as a simplified way to account for the fact that otherwise these quantities would be inflated by the measurement errors. As for the other properties, Phoenix II is the system with the best constrained values.

From the Galactocentric velocities we also derive estimates of the orbital poles. These are shown in Figure 9: in many cases the error in proper motion is rather large, making nearly a great circle possible. The poles of Columba I and Reticulum III are not well localized, the one σ interval extends over more than one third of a great circle for Columba I and over 75° for Reticulum III. In the case of Reticulum III, the LMC is within 3° from the great circle allowed by the MonteCarlo simulations, but only in a minority of cases; on the other hand, for Col I, even with the large errors, the direction of the orbital pole is always at least

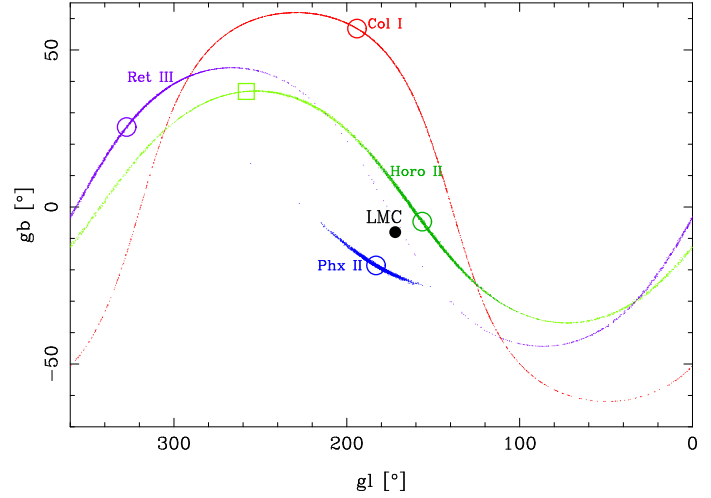


Fig. 9. All-sky view of orbital poles for the objects in the sample; the open circles (or square) indicate the value which follows from the measurements while the small points around each object plot the orbital poles from the 2000 individual Monte Carlo simulations. We show for all galaxies our preferred membership selection; for Horo II, we also show the other option in light green, which covers nearly the full great circle. For the other satellites the two options lead to very similar results.

32° from the LMC one. It is therefore less likely that these two objects were associated with the LMC.

The most likely pole of Horologium II is formally determined with a higher accuracy, $l = 156 \pm 17$ and $b = -5 \pm 12$ degree, and it is at 16 degree distance of the LMC. An association of Horo II to the LMC depends critically on whether the brightest (most distant in r_{half}) candidate member is truly a member or not. When excluding it, the pole direction changes very significantly ($l = 258$ and $b = 37$) and the one sigma region spans nearly two thirds of the sky. In either of the two cases we cannot exclude that the direction of its orbital pole is close to the one of the LMC.

Phoenix II has the best localized pole direction: $l = 185 \pm 9$ and $b = -18 \pm 3$ degree, which is at 16° from the pole of the LMC, see Figure 9.

The total velocities are mostly high given the distance of the galaxies, partly larger than the escape speed in a low mass halo ($0.8 \times 10^{12} M_\odot$) like that used in Fritz et al. (2018). That could be an argument for accretion with high angular momentum, as in case of the LMC. However, we note that most proper motions have large errors, and thus the total velocity has a large value. Phoenix II is the best measured galaxy with $V_{3D} = 258 \pm 67$ km/s, although still larger than the circular velocity at its dis-

tance. Horologium II has the second smallest error (~ 99 km/s) and a really large velocity of about 390 km/s in our preferred case. Still, since the value of the total velocity of Horo II depends strongly on the sample of members used, we cannot be certain of whether it is on a high angular momentum orbit or not. The errors on the total velocity of the other objects are so large that the results are not biased.

Our determinations of the systemic proper motions and line-of-sight velocities, combined to the galaxies's distance, give us the opportunity of exploring a possible origin as former LMC satellites; we compare to the predictions given by Jethwa et al. (2016) and Kallivayalil et al. (2018) since they are in observables space, which avoids the issues of error propagation onto the Galactocentric velocities.

For Horo II, in the case of the generous membership sample, our measurements match very well the predictions by Kallivayalil et al. (2018) but not those by Jethwa et al. (2016). On the other hand, the estimate from the sample of very likely members is compatible within $1-2\sigma$ with both studies, given the larger error-bars.

Reticulum III matches the predictions by Jethwa et al. (2016) in all quantities within $1-2\sigma$ both for an association to the LMC or to the SMC. It also agrees well with the model in Kallivayalil et al. (2018) in μ_δ and v_{helio} , but not in μ_α **.

For Columba I the agreement is good in the proper motions with both models which is partly caused by the large errors of the observations but entirely off in line-of-sight velocity for Kallivayalil et al. (2018) and compatible with Jethwa et al. (2016) within 2σ . We point out thought that the typical error-bars in the line-of-sight heliocentric systemic velocity by the latter authors are very large for all galaxies, at least $\pm 70-80$ km/s.

As mentioned in the previous section, we recover closely the proper motion of Phoenix II deduced by Kallivayalil et al. (2018)⁴; however, our systemic line-of-sight velocity is off by 45 km/s, about 9σ away from their prediction, which is $-15.5^{+5.2}_{-10.5}$ (here, σ is the error in the predicted line-of-sight velocity). Our measurements do not agree with Jethwa et al. (2016) model predictions.

Phoenix II orbital pole is close to the location of the pole of Hydra I a galaxy considered to be a satellite in Kallivayalil et al. (2018). The other two galaxies have large errors in the proper motion and thus membership does not seem fully impossible from the motions alone. Since Columba I is located outside the main track of LMC debris and has an unfitting large distance for its location, we think that it is very unlikely that it is a former member.

We conclude that Phoenix II is the only object for which the firm case of a former association to the LMC can be made; the problems in Kallivayalil et al. (2018) to predict the properties exactly could be associated with the fact that they use a light-LMC analog.

Jethwa et al. (2016) consider a range of usually more massive analogs in set up simulations, which result in much larger ranges of predicted properties than Kallivayalil et al. (2018). Still, the ranges given by Jethwa et al. (2016) and Kallivayalil et al. (2018) differ, especially for the proper motions. There are several possible reasons for that. It might be that the difference in the LMC mass is responsible for the difference, but it is also possible that other more subtle effects are responsible like differences in the conversion into the solar reference frame.

5. Summary and conclusions

We present results from FLAMES/GIRAFFE intermediate resolution spectroscopy in the region 8200-9200Å for individual stars in the line-of-sight to four of the newly discovered Milky Way satellites that are lacking spectroscopic information in the literature: Columba I, Horologium II, Phoenix II and Reticulum III. This implies that their nature as globular clusters or dwarf galaxies was not established and even basic properties such as their systemic line-of-sight velocity were unknown. Horologium II and Reticulum III also lack determinations of their systemic proper motion, while for Columba I and Phoenix II the only existing determination was obtained by K18 searching the proper motion space assuming that these objects would have been prior satellites of the LMC, guided by a "light LMC" N-body model.

A spectral fitting analysis is performed in order to extract the line-of-sight velocity and metallicity of the target stars, assuming photometric estimates of the stars's effective temperature and gravity. The information coming from the spectroscopy is used together with Gaia DR2 astrometric data and photometry (also from the DeCam NSC DR1 catalogue) to search for stars that are probable members to these systems. All the velocity peaks that we associate to detections of member stars in these systems are found to be highly unlikely to be due to polluter stars passing our selection criteria.

Once the systemic velocity of the system is known, additional members are looked for among the stars targetted by FLAMES/GIRAFFE but without Gaia DR2 kinematic informations. In total we find 12 very likely members (2 in Col I, 2 in Horo II, 5 in Phx II, 3 in Ret III) at most within $2.1 r_{\text{half}}$. In addition we have 5 candidate member stars (3 for Col I, 1 for Horo II and 1 for Phx II), usually at larger distances.

The system with the most constrained properties is Phoenix II; for this object, we resolve its line-of-sight velocity dispersion ($7.1^{+1.5}_{-1.1}$ and $8.2^{+1.9}_{-1.5}$ km/s, for the generous and strict membership selection, respectively); we also find an intrinsic metallicity spread of at least $0.34^{+0.07}_{-0.05}$ dex; these properties suggest its nature as a dwarf galaxy. The results on the other systems are more sensitive to the adopted sample, and we cannot robustly place the objects in one category or another one. Nonetheless, should these three objects be globular clusters, being in the outer halo, they might have formed within an accreted dwarf system and therefore still provide information on their former host, such as e.g. its orbital properties.

Along the great circle track allowed by the measurement errors, Columba I orbital pole remains always at least 32° from the LMC, making an association unlikely. On the other hand, we cannot firmly exclude an association between the LMC and Horo II or Ret III, although the latter appears rather unlikely due to the small fraction of MonteCarlo realizations that could bring its orbital pole close to the one of the LMC.

The orbital pole of Phoenix II is about 16° away from the one of the LMC, and it is a promising system for having been a former LMC satellite. Its proper motion agrees well with the predictions by K18, although the line-of-sight systemic velocity is 9σ away. However, it is possible that a LMC-analog producing a larger spread in the tidal debris properties would lead to a better agreement also in this observable. Given the similarity of the LMC and Vast Polar Structure orbital pole, this also implies that

⁴ For this galaxy the authors guide their systemic proper motion determination by searching for a clump in proper motion space in the region predicted by the model.

Phoenix II could be part of this structure (e.g. Pawłowski et al. 2012).

Acknowledgements. This work has made use of data from the European Space Agency (ESA) mission *Gaia* (<https://www.cosmos.esa.int/gaia>), processed by the *Gaia* Data Processing and Analysis Consortium (DPAC, <https://www.cosmos.esa.int/web/gaia/dpac/consortium>). Funding for the DPAC has been provided by national institutions, in particular the institutions participating in the *Gaia* Multilateral Agreement. G.B. gratefully acknowledges financial support by the Spanish Ministry of Economy and Competitiveness (MINECO) under the Ramon y Cajal Programme (RYC-2012-11537) and the grant AYA2014-56795-P.

References

Allende Prieto, C., Beers, T. C., Wilhelm, R., et al. 2006, ApJ, 636, 804

Allende Prieto, C., Koesterke, L., Hubeny, I., et al. 2018, A&A, 0 [arXiv: submitted]

Amorisco, N. C., Evans, N. W., & van de Ven, G. 2014, Nature, 507, 335

Annibali, F., Nipoti, C., Ciotti, L., et al. 2016, ApJ, 826, L27

Bechtol, K., Drlica-Wagner, A., Balbinot, E., et al. 2015, ApJ, 807, 50

Bressan, A., Marigo, P., Girardi, L., et al. 2012, MNRAS, 427, 127

Bullock, J. S. & Boylan-Kolchin, M. 2017, ARA&A, 55, 343

Carlin, J. L., Grillmair, C. J., Muñoz, R. R., Nidever, D. L., & Majewski, S. R. 2009, ApJ, 702, L9

Carlin, J. L., Sand, D. J., Muñoz, R. R., et al. 2017, AJ, 154, 267

Carrera, R., Rodríguez Espinosa, L., Casamiquela, L., et al. 2017, MNRAS, 470, 4285

da Silva, L., Girardi, L., Pasquini, L., et al. 2006, A&A, 458, 609

Deason, A. J., Belokurov, V., Koposov, S. E., & Rockosi, C. M. 2014, ApJ, 787, 30

Deason, A. J., Wetzel, A. R., Garrison-Kimmel, S., & Belokurov, V. 2015, MNRAS, 453, 3568

Dooley, G. A., Peter, A. H. G., Carlin, J. L., et al. 2017, MNRAS, 472, 1060

Drlica-Wagner, A., Bechtol, K., Rykoff, E. S., et al. 2015a, ApJ, 813, 109

Drlica-Wagner, A., Bechtol, K., Rykoff, E. S., et al. 2015b, ApJ, 813, 109

Evans, D. W., Riello, M., De Angelis, F., et al. 2018, ArXiv e-prints [arXiv: 1804.09368]

Frebel, A., Simon, J. D., & Kirby, E. N. 2014, ApJ, 786, 74

Fritz, T. K., Battaglia, G., Pawłowski, M. S., et al. 2018, ArXiv e-prints [arXiv: 1805.00908]

Fritz, T. K., Linden, S. T., Zivick, P., et al. 2017a, ApJ, 840, 30

Fritz, T. K., Lokken, M., Kallivayalil, N., et al. 2017b, ArXiv e-prints [arXiv: 1711.09097]

Gaia Collaboration, Brown, A. G. A., Vallenari, A., et al. 2018a, ArXiv e-prints [arXiv: 1804.09365]

Gaia Collaboration, Helmi, A., van Leeuwen, F., et al. 2018b, ArXiv e-prints [arXiv: 1804.09381]

Gaia Collaboration, Prusti, T., de Bruijne, J. H. J., et al. 2016, A&A, 595, A1

Garrison-Kimmel, S., Bullock, J. S., Boylan-Kolchin, M., & Bardwell, E. 2017, MNRAS, 464, 3108

Jethwa, P., Erkal, D., & Belokurov, V. 2016, MNRAS, 461, 2212

Kallivayalil, N., Sales, L., Zivick, P., et al. 2018, ArXiv e-prints [arXiv: 1805.01448]

Kim, D. & Jerjen, H. 2015, ApJ, 808, L39

Kim, D., Jerjen, H., Geha, M., et al. 2016, ApJ, 833, 16

Kim, D., Jerjen, H., Milone, A. P., Mackey, D., & Da Costa, G. S. 2015, ApJ, 803, 63

Kirby, E. N., Boylan-Kolchin, M., Cohen, J. G., et al. 2013, ApJ, 770, 16

Kirby, E. N., Cohen, J. G., Simon, J. D., et al. 2017, ApJ, 838, 83

Kirby, E. N., Simon, J. D., & Cohen, J. G. 2015, ApJ, 810, 56

Koch, A., Wilkinson, M. I., Kleyne, J. T., et al. 2009, ApJ, 690, 453

Koposov, S. E., Belokurov, V., Torrealba, G., & Evans, N. W. 2015a, ApJ, 805, 130

Koposov, S. E., Casey, A. R., Belokurov, V., et al. 2015b, ApJ, 811, 62

Koposov, S. E., Walker, M. G., Belokurov, V., et al. 2018, ArXiv e-prints [arXiv: 1804.06430]

Laevens, B. P. M., Martin, N. F., Bernard, E. J., et al. 2015, ApJ, 813, 44

Li, T. S., Simon, J. D., Drlica-Wagner, A., et al. 2017, ApJ, 838, 8

Li, T. S., Simon, J. D., Kuehn, K., et al. 2018a, ArXiv e-prints [arXiv: 1804.07761]

Li, T. S., Simon, J. D., Pace, A. B., et al. 2018b, ArXiv e-prints [arXiv: 1802.06810]

Lindgren, L., Hernandez, J., Bombrun, A., et al. 2018, ArXiv e-prints [arXiv: 1804.09366]

Martin, N. F., Geha, M., Ibata, R. A., et al. 2016, MNRAS, 458, L59

Martin, N. F., Ibata, R. A., Chapman, S. C., Irwin, M., & Lewis, G. F. 2007, MNRAS, 380, 281

Martin, N. F., Nidever, D. L., Besla, G., et al. 2015, ApJ, 804, L5

Mashonkina, L., Jablonka, P., Sitnova, T., Pakhomov, Y., & North, P. 2017, A&A, 608, A89

Massari, D. & Helmi, A. 2018, ArXiv e-prints [arXiv: 1805.01839]

McConnachie, A. W. & Côté, P. 2010, ApJ, 722, L209

Melo, C., Primas, F., Pasquini, L., Patat, F., & Smoker, J. 2009, The Messenger, 135, 17

Muratov, A. L. & Gnedin, O. Y. 2010, ApJ, 718, 1266

Mutlu-Pakdil, B., Sand, D. J., Carlin, J. L., et al. 2018, ArXiv e-prints [arXiv: 1804.08627]

Nidever, D. L., Dey, A., Olsen, K., et al. 2018, ArXiv e-prints [arXiv: 1801.01885]

Pasquini, L., Avila, G., Blecha, A., et al. 2002, The Messenger, 110, 1

Pawłowski, M. S., Pflamm-Altenburg, J., & Kroupa, P. 2012, MNRAS, 423, 1109

Ramírez, I. & Meléndez, J. 2005, ApJ, 626, 465

Revaz, Y. & Jablonka, P. 2018, ArXiv e-prints [arXiv: 1801.06222]

Rich, R. M., Collins, M. L. M., Black, C. M., et al. 2012, Nature, 482, 192

Rybicki, J., Demleitner, M., Fouesneau, M., et al. 2018, ArXiv e-prints [arXiv: 1804.01427]

Sales, L. V., Navarro, J. F., Cooper, A. P., et al. 2011, MNRAS, 418, 648

Sales, L. V., Navarro, J. F., Kallivayalil, N., & Frenk, C. S. 2017, MNRAS, 465, 1879

Sand, D. J., Crnojević, D., Strader, J., et al. 2014, ApJ, 793, L7

Sand, D. J., Spekkens, K., Crnojević, D., et al. 2015, ApJ, 812, L13

Simon, J. D. 2018, ArXiv e-prints [arXiv: 1804.10230]

Simon, J. D., Drlica-Wagner, A., Li, T. S., et al. 2015, ApJ, 808, 95

Simon, J. D. & Geha, M. 2007, ApJ, 670, 313

Simon, J. D., Geha, M., Minor, Q. E., et al. 2011, ApJ, 733, 46

Simon, J. D., Li, T. S., Drlica-Wagner, A., et al. 2017, ApJ, 838, 11

Toloba, E., Sand, D. J., Spekkens, K., et al. 2016, ApJ, 816, L5

Torrealba, G., Belokurov, V., Koposov, S. E., et al. 2018, MNRAS, 475, 5085

Torrealba, G., Koposov, S. E., Belokurov, V., & Irwin, M. 2016, MNRAS, 459, 2370

van der Marel, R. P. & Kallivayalil, N. 2014, ApJ, 781, 121

Walker, M. G., Belokurov, V., Evans, N. W., et al. 2009, ApJ, 694, L144

Walker, M. G., Mateo, M., Olszewski, E. W., et al. 2016, ApJ, 819, 53

Weisz, D. R., Koposov, S. E., Dolphin, A. E., et al. 2016, ApJ, 822, 32

Willman, B., Geha, M., Strader, J., et al. 2011, AJ, 142, 128

Willman, B. & Strader, J. 2012, AJ, 144, 76

Yozin, C. & Bekki, K. 2015, MNRAS, 453, 2302

Zinn, R. 1993, in Astronomical Society of the Pacific Conference Series, Vol. 48, The Globular Cluster-Galaxy Connection, ed. G. H. Smith & J. P. Brodie, 38